

Explicit Second-order LiDAR Bundle Adjustment Algorithm Using Mean Squared Group Metric

Tingchen Ma, Yongsheng Ou* and Sheng Xu*

Abstract—The Bundle Adjustment (BA) algorithm is a widely used nonlinear optimization technique in the backend of Simultaneous Localization and Mapping (SLAM) systems. By leveraging the co-view relationships of landmarks from multiple perspectives, it constructs a joint estimation model for both poses and landmarks, enabling the system to generate refined maps and reduce front-end localization errors. However, applying BA to LiDAR data presents unique challenges due to the large volume of 3D points typically present in point clouds, making robust and accurate model solving more complex. In this work, we propose a novel mean square group metric (MSGM). This metric applies mean square transformation to uniformly process the measurement of plane landmarks from a single perspective. The transformed metric ensures scale interpretability while avoiding the time-consuming point-by-point calculations. By integrating a robust kernel function, the metrics involved in the BA model are reweighted, enhancing the robustness of the solution process. On the basis of the proposed robust LiDAR BA model, we derived an explicit second-order estimator (RSO-BA). This estimator employs analytical formulas for Hessian and gradient calculations, ensuring the precision of the BA solution. We evaluated the proposed RSO-BA estimator against existing implicit second-order and explicit approximate second-order estimators using the publicly available datasets. The experimental results demonstrate that the RSO-BA estimator outperforms its counterparts regarding registration accuracy and robustness, particularly in large-scale or complex unstructured environments.

Index Terms—Explicit LiDAR bundle adjustment, Mean square group metric, Robust kernel function, Second-order state estimation

I. INTRODUCTION

Light detection and ranging (LiDAR) is a three-dimensional scanning sensor with the continuous-time sampling characteristic. It is widely used in geographic surveying, urban monitoring, mobile robots (including unmanned aerial vehicles, autonomous driving) and various other fields. In mobile robots, LiDAR-based SLAM (Simultaneous Localization and Mapping) systems are crucial for constructing accurate 3D

maps of the environment and ensuring robust positioning. Currently, LiDAR SLAM systems can be broadly categorized into two main approaches: direct methods and feature-based methods.

LiDAR SLAM systems based on direct methods, such as [1], [2] utilize grid downsampling to process measurement point clouds. By reducing the resolution of the point clouds, these systems require less computation, enabling real-time positioning and mapping. Specifically, each current LiDAR frame undergoes a scan-to-model registration process for pose estimation. Then, the point cloud will be transformed into the map coordinate system and used to update the point-based map (relative to the feature-based map). In the above scheme, the minimum unit of the map model is a single 3D point. However, due to the sparsity of sampled LiDAR data, it is challenging to consistently hit the same spatial position across consecutive frames. As a result, point-based Bundle Adjustment (BA) algorithms are not applicable in such systems. On the other hand, feature-based LiDAR SLAM systems employ techniques like scanline smoothness [3]–[5], voxel segmentation [6], [7] and region growing [8], [9] to extract structured edge and surface feature point sets from measurement point clouds. These extracted features are then used to accomplish localization and mapping tasks. Compared to 3D points, stable data correlation between frames is more easily obtained for structural feature landmarks. LiDAR BA technology based on structural features has seen significant advancements in recent years.

Some studies [8]–[10] have designed LiDAR BA models in a form similar to visual BA [11] (referred to as explicit BA in this paper). During state estimation, all participating landmarks and robot poses are updated simultaneously, with the Schur complement technique often employed to accelerate the solution of the explicit BA model. In contrast, other approaches [6], [7] decompose the standard BA problem into two steps: eigenvalue fitting and multi-view pose registration (defined here as implicit BA). Unlike explicit BA schemes, [6], [7] derived a second-order estimator using the analytical Hessian matrix and gradient vector, resulting in higher estimation accuracy. In the latest developments on two types of schemes [9] and [7], the concept of “point clustering” has been introduced to avoid point-based operations during the solving process of linear systems, thereby improving computational efficiency. The error metric constructed based on the point clustering matrix equals the sum of error metrics corresponding to all measurement points that make up the matrix. Consequently, these schemes treat all landmarks equally during the BA-solving process. However, in practical

This work was supported by the National Key Research and Development Program of China under Grant 2018AAA0103001; in part by the National Natural Science Foundation of China (Grants No. U1813208, 62173319, 62063006); in part by the Guangdong Basic and Applied Basic Research Foundation (2020B1515120054); in part by the Shenzhen Fundamental Research Program (JCYJ20200109115610172).

* Corresponding author, e-mail: ys.ou@siat.ac.cn.

Tingchen Ma is with the Shenzhen Institute of Advanced Technology, Chinese Academy of Sciences, Shenzhen 518055, China, and also with the Shenzhen College of Advanced Technology, University of Chinese Academy of Sciences, Shenzhen 518055, China.

Yongsheng Ou is with the Guangdong Provincial Key Lab of Robotics and Intelligent System, Shenzhen Institute of Advanced Technology, Chinese Academy of Sciences, Shenzhen 518055, China

scenarios, applying appropriate weighting to the metric (using robust kernel functions [12]) can significantly improve the system’s accuracy and adaptability in complex environments. Additionally, in the two-step solution method proposed by implicit BA, eigenvalue fitting depends on the initial value (provided by the front end) or the pose estimation result from the previous iteration, which may negatively impact the robustness and accuracy of the solution.

In response to the above challenges, we propose a novel BA estimator to achieve high-precision map refinement in the backend of LiDAR SLAM systems. The key contributions of this article are as follows:

- We introduce a novel MSGM that considers the number of measurement points during its construction, ensuring the interpretability of scale. This metric allows for developing a robust LiDAR BA model by incorporating robust kernel functions.
- We derived the analytical Hessian matrix and gradient vector required for solving the explicit second-order BA estimator. The RSO-BA is then integrated into the LiDAR SLAM system for thorough algorithm evaluation.

II. RELATED WORK

A. Point Cloud Registration

Point cloud registration is a fundamental technique in the field of 3D vision. It aims to estimate the 3/6 degree of freedom pose transformation between the current frame point cloud and the target model (whether another point cloud or a map) through data association. The ICP [13] algorithm employs nearest neighbor search to update data associations iteratively, refining the state estimation until the error converges. While the ICP algorithm is highly generalizable, it requires a certain level of point cloud density in both the frame and the model. Considering the universality of surface features, Chen et al. [14] proposed a point-to-plane registration algorithm. This approach derives surface features by fitting the local point set in the target model using principal component analysis (PCA) [15]. The G-ICP [16] algorithm considers using the current and target point covariance distribution during registration, enabling robust performance even in unstructured environments. Further enhancements, such as the VG-ICP [17] and N-ICP [18] algorithms, introduce multi-distribution modeling and normal vector constraints, respectively, thereby improving registration accuracy.

As a commonly used 3D scanning sensor, Lidar has the characteristic of continuous time sampling. When the LiDAR is in motion, distortion is inevitably introduced to the measurement point cloud. Directly applying traditional registration algorithms to such distorted data can result in significant state estimation errors. To address this issue, Zhang et al. [4] proposed assuming uniform motion of the robot during the point cloud frame sampling process. In scan-to-scan registration, linear interpolation compensates for motion distortion in the point cloud. Dellenbach et al. [2] proposed a CT-ICP algorithm that simultaneously estimates the beginning and end states of a point cloud frame. This algorithm uses linear and spherical interpolation methods to handle translation and

quaternion components. Point clouds containing distortions can be directly registered to the map.

As a high-frequency internal sensor, the Inertial Measurement Unit (IMU) can complement LiDAR well [19]. Frameworks like [1] utilize IMU-based bidirectional propagation algorithms to preprocess point cloud distortions. The IEKF [20] algorithm is then employed to complete state estimation. Typically, undistorted LiDAR point clouds and single-frame pose estimation can be used as initial values for the Bundle Adjustment (BA) problem. In the LiDAR SLAM backend, the BA algorithm, which considers the co-view constraint of landmarks, is used to generate higher-precision map models.

B. Bundle Adjustment

The bundle adjustment [11] algorithm is widely used in 3D reconstruction and SLAM. It leverages the co-view constraints of landmarks to construct a joint estimation model for both landmarks and multi-frame poses, allowing for the refinement of the local map. Initially, BA algorithms were primarily used in 3D vision, where spatial points, edges, and planes are re-projected onto 2D images to obtain error metrics for the BA model. To address mismatches, kernel functions such as Huber [21], and Cauchy [22] are employed to reweight the error metrics, resulting in a more robust BA model. This robust BA technology has been integrated into many open-source visual SLAM [23], [24] systems. On the other hand, the standard BA model often requires simultaneous estimation of thousands of landmark parameters, which can be computationally intensive. To expedite the solution of the normal equations, the Schur complement technique is frequently used, as seen in the open-source library like g2o [25].

Unlike visual BA algorithms, the LiDAR BA algorithms face more challenges due to the unique sampling method of the sensor. Geneva et al. [10] proposed a plane-to-plane error metric to construct the BA model. Before solving the BA model, the plane landmark measurements are obtained by processing the local point cloud in the LiDAR coordinate system using the PCA fitting algorithm. The plane-to-plane error metric avoids point-by-point calculations during BA solving, leading to high computational efficiency. Furthermore, Zhou et al. [8] conducted a theoretical analysis comparing point-to-plane and plane-to-plane error metrics, with experimental results confirming that point-to-plane error metrics offer higher estimation accuracy. In related works [7], [9], methods based on "point clustering" have been proposed to process all measurement points for landmarks from each perspective. This approach makes the time complexity of the BA problem dependent only on the size of the sliding window and the number of landmarks involved in optimization. The BA problem is solved using an approximate second-order method based on Gauss-Newton [26].

Considering the specific structure of LiDAR BA models, which are based on edge and surface landmarks, some studies [6], [7] have proposed efficient two-step iterative solution schemes. These schemes sequentially perform eigenvalue fitting and multi-view registration to refine the map. Unlike the explicit BA scheme, the model dimensions of implicit BA are

only related to the number of keyframes in the sliding window. However, the eigenvalue fitting step theoretically overlooks the impact of pose updates during each iteration, potentially leading to a loss of estimation accuracy. Additionally, while "point clustering" can enhance the solution efficiency of the BA model, it sacrifices scale interpretability in the corresponding error metric, making robust BA techniques unusable and introducing potential risks in estimation. To address these issues, we proposed a novel mean square group metric that maintains scale interpretability, allowing for the construction of robust BA models. We also derived an explicit second-order estimator for solving the robust BA model. The proposed estimator performs robustly and accurately in complex scenarios.

III. METHOD

A. Problem Formulation

Assume the map coordinate system is denoted as m , and the measurement point cloud obtained by the LiDAR is defined in the LiDAR coordinate system l . The backend of the LiDAR SLAM system maintains a sliding window containing N_w keyframes. The pose of keyframe \mathbb{F}_i in the map coordinate system is represented as $\mathbf{T}_i \in \text{SE}(3)$. The set of poses within the sliding window can be denoted as $\chi = \{\mathbf{T}_i\}_{i=1}^{N_w}$.

The set of plane landmark (the most common feature in the environment) observed by keyframe \mathbb{F}_i is denoted as $\Gamma_i = \{\pi_j\}_{j=1}^{N_i}$. The 3D measurement point set corresponding to each landmark π_j is represented as $\mathbf{F}_j = \{\mathbf{p}_{j,o}^m\}_{o=1}^{N_j^f}$. Each plane landmark maintains a fixed set $\mathbf{F}_j = \{\mathbf{p}_{j,o}^m\}_{o=1}^{N_j^f}$ in the map coordinate system. The points in \mathbf{F}_j are obtained by transforming local measurements to the map coordinate system when a keyframe exits the sliding window. Assuming $\tilde{\mathbf{p}}_{i,j,k}^l$ and $\tilde{\mathbf{p}}_{j,o}^m$ are homogeneous coordinates of $\mathbf{p}_{i,j,k}^l$ and $\mathbf{p}_{j,o}^m$, respectively, we can define the distance $e_{i,j,k}$ from a local measurement point $\tilde{\mathbf{p}}_{i,j,k}^l$ to the plane landmark π_j

$$e_{i,j,k} = \pi_j^T \mathbf{T}_i \tilde{\mathbf{p}}_{i,j,k}^l = \tilde{\mathbf{p}}_{i,j,k}^{l T} \mathbf{T}_i^T \pi_j. \quad (1)$$

The distance from a fixed map point to the plane landmark is given by

$$e_{j,o}^f = \pi_j^T \tilde{\mathbf{p}}_{j,o}^m = \tilde{\mathbf{p}}_{j,o}^{m T} \pi_j. \quad (2)$$

Where, the plane landmark is represented by $\pi_j = [\mathbf{n}_j, d_j]^T$, with $\mathbf{n}_j = [n_{j,x}, n_{j,y}, n_{j,z}]^T$ as its normal vector, d_j as the distance from the origin to the plane. Assuming that set $\mathbf{\Pi} = \{\pi_q\}_{q=1}^{N_w}$ contains all effective plane landmarks within the sliding window. The standard BA model can be denoted as

$$C = \arg \min_{\mathbf{X}} \sum_{i=1}^{N_w} \sum_{j=1}^{N_i} \sum_{k=1}^{N_j} \|e_{i,j,k}\|_2^2 + \sum_{j=1}^{N_i} \sum_{o=1}^{N_j^f} \|e_{j,o}^f\|_2^2, \quad (3)$$

where, $\mathbf{X} = \{\chi, \mathbf{\Pi}\}$ represent all the optimized variables in the formula (3). In Section III.A, we introduce a robust LiDAR BA model considering the kernel function. Section III.B further derives an explicit second-order estimator for solving these robust BA models.

B. Mean Square Group Metric and Robust LiDAR BA Model

Given the local measurement point set $Z_{i,j} = \{\mathbf{p}_{i,j,k}^l\}_{k=1}^{N_{i,j}}$ and the fixed point set $\mathbf{F}_j = \{\mathbf{p}_{j,o}^m\}_{o=1}^{N_j^f}$ of landmark π_j at keyframe \mathbb{F}_i , we can organize $Z_{i,j}$ into the column vector $\mathbf{P}_{i,j} = [\dots, \tilde{\mathbf{p}}_{i,j,k}^l, \dots]^T$ and \mathbf{F}_j into the column vector $\mathbf{P}_j = [\dots, \tilde{\mathbf{p}}_{j,o}^m, \dots]^T$. This allows us to equivalently express formula (3) in the following form [] for a more efficient solution

$$C = \arg \min_{\mathbf{X}} \sum_{i=1}^{N_w} \sum_{j=1}^{N_i} c_{i,j} + \sum_{j=1}^{N_i} c_j, \quad (4)$$

where, $c_{i,j} = \pi_j^T \mathbf{T}_i \mathbf{Q}_{i,j} \mathbf{T}_i^T \pi_j$ represents the integrated group metric and $c_j = \pi_j^T \mathbf{M}_j \pi_j$ denotes the fixed group metric. The integrated group matrix $\mathbf{Q}_{i,j}$ and fixed group matrix \mathbf{M}_j are defined as follows

$$\mathbf{Q}_{i,j} = \mathbf{P}_{i,j}^T \mathbf{P}_{i,j} \quad (5)$$

$$\mathbf{M}_j = \mathbf{P}_j^T \mathbf{P}_j \quad (6)$$

For the standard BA model corresponding to formula (3), we can enhance the robustness of the estimation model by applying a robust kernel function to each point-to-plane error metric. However, the error metrics $c_{i,j}$ and c_j in formula (4) compromise scale interpretability due to the use of the group matrix, making it difficult to determine the appropriate threshold for the robust kernel function. Therefore, we introduce the number of measurement points to adjust $c_{i,j}$ and c_j . The robust BA model is then constructed as follows

$$C' = \arg \min_{\mathbf{X}} \sum_{i=1}^{N_w} \sum_{j=1}^{N_i} \rho(c_{i,j}/N_{i,j}) + \sum_{j=1}^{N_i} \rho(c_j/N_j^f), \quad (7)$$

where, $\rho(\cdot)$ represents the robust kernel function. In this paper, the Huber kernel function is used for the subsequent related experiments. The integrated mean square group metric $c'_{i,j}$ and the fixed mean square group metric c'_j are defined as follows

$$c'_{i,j} = c_{i,j}/N_{i,j} \quad (8)$$

$$c'_j = c_j/N_j^f \quad (9)$$

Essentially, $c'_{i,j}$ calculates the mean square of all measurement point-to-plane errors generated by the plane landmark π_j at keyframe \mathbb{F}_i . Similarly, c'_j is the mean square calculation of all fixed point-to-plane errors for the plane landmark π_j . Next, we will derive an explicit second-order estimator to solve formula (7).

C. Explicit Second-order Estimator

Using the integrated mean square group metric $\rho(c'_{i,j})$ and fixed mean square group metric $\rho(c'_j)$ with robust kernel functions as examples, this section will derive the hessian matrix and gradient vector required for solving the explicit second-order estimator. Initially, we ignore the effect of $\rho(\cdot)$ and parameterize the estimated values of the mean square group metric $c'_{i,j}$ as

$\mathbf{x}_{i,j} = [t_{i,x}, t_{i,y}, t_{i,z}, \varphi_{i,x}, \varphi_{i,y}, \varphi_{i,z}, \Pi_{j,1}, \Pi_{j,2}, \Pi_{j,3}]^T = [x_1, x_2, x_3, x_4, x_5, x_6, x_7, x_8, x_9]$. For a given pose $\mathbf{T}_i = \begin{bmatrix} \mathbf{R}_i & \mathbf{t}_i \\ 0 & 1 \end{bmatrix} \in \text{SE}(3)$, its rotational component $\mathbf{R}_i \in \text{SO}(3)$ can be represented using Euler angles

$$\mathbf{R}_i = \mathbf{R}_x \mathbf{R}_y \mathbf{R}_z = \begin{bmatrix} c_y c_z & -c_y s_z & s_y \\ c_x s_z + s_x s_y c_z & c_x c_z - s_x s_y s_z & -s_x c_y \\ s_x s_z - c_x s_y c_z & c_x s_y s_z + s_x c_z & c_x c_y \end{bmatrix}. \quad (10)$$

where, $s_x, s_y, s_z, c_x, c_y, c_z$ are the abbreviation of $\sin(\varphi_{i,x}), \sin(\varphi_{i,y}), \sin(\varphi_{i,z}), \cos(\varphi_{i,x}), \cos(\varphi_{i,y}), \cos(\varphi_{i,z})$. $\mathbf{t}_i \in \mathbb{R}^3$ is the translation component of \mathbf{T}_i . $\mathbf{\Pi}_j = [\Pi_{j,1}, \Pi_{j,2}, \Pi_{j,3}]^T$ is the closest point representation [10] of plane landmark π_j . Let $\pi'_{i,j} = \mathbf{T}_i^T \pi_j$, $c'_{i,j}$ can be rephrased as

$$c'_{i,j} = \pi'^T_{i,j} \mathbf{Q}_{i,j} \pi'_{i,j} / N_{i,j} \quad (11)$$

The gradient vector $\mathbf{g}_{i,j} = [\dots g_{i,j}^k \dots]^T_{9 \times 1}$ can be obtained by calculating the first-order partial derivative of $c'_{i,j}$ with respect to $\mathbf{x}_{i,j}$

$$g_{i,j}^k = \frac{\partial c'_{i,j}}{\partial x_k} = \frac{2}{N_{i,j}} \pi'^T_{i,j} \mathbf{Q}_{i,j} \frac{\partial \pi'_{i,j}}{\partial x_k} \quad (12)$$

$$\text{Hessian matrix } \mathbf{H}_{i,j} = \begin{bmatrix} \ddots & \vdots & \vdots \\ \dots & H_{i,j}^{k,l} & \dots \\ \vdots & \vdots & \ddots \end{bmatrix}_{9 \times 9}$$

is obtained by taking the second-order partial derivative of $c'_{i,j}$ with respect to $\mathbf{x}_{i,j}$

$$H_{i,j}^{k,l} = \frac{\partial^2 c'_{i,j}}{\partial x_k \partial x_l} = \frac{2}{N_{i,j}} \left(\frac{\partial \pi'_{i,j}}{\partial x_l} \mathbf{Q}_{i,j} \frac{\partial \pi'_{i,j}}{\partial x_k} + \pi'^T_{i,j} \mathbf{Q}_{i,j} \frac{\partial^2 \pi'_{i,j}}{\partial x_k \partial x_l} \right) \quad (13)$$

Before deriving $\frac{\partial \pi'_{i,j}}{\partial x_k}$, we first obtain \mathbf{R}_i^T according to the definition of $\mathbf{R}_i = \mathbf{R}_x \mathbf{R}_y \mathbf{R}_z$

$$\mathbf{R}_i^T = \begin{bmatrix} c_y c_z & c_x s_z + s_x s_y c_z & s_x s_z - c_x s_y c_z \\ -c_y s_z & c_x c_z - s_x s_y s_z & c_x s_y s_z + s_x c_z \\ s_y & -s_x c_y & c_x c_y \end{bmatrix}. \quad (14)$$

Substituting the above formula into $\pi'_{i,j}$, we obtain

$$\pi'_{i,j} = \mathbf{T}_i^T \pi_j = \begin{bmatrix} \mathbf{R}_i^T & 0 \\ \mathbf{t}_i^T & 1 \end{bmatrix} \begin{bmatrix} \mathbf{n}_j \\ d_j \end{bmatrix} = \begin{bmatrix} \mathbf{R}_i^T \mathbf{n}_j \\ \mathbf{t}_i^T \mathbf{n}_j + d_j \end{bmatrix} = \begin{bmatrix} n_{j,x}(c_y c_z) + n_{j,y}(c_x s_z + s_x s_y c_z) + n_{j,z}(s_x s_z - c_x s_y c_z) \\ n_{j,x}(-c_y s_z) + n_{j,y}(c_x c_z - s_x s_y s_z) + n_{j,z}(c_x s_y s_z + s_x c_z) \\ n_{j,x}(s_y) + n_{j,y}(-s_x c_y) + n_{j,z}(c_x c_y) \\ t_{i,x} n_{j,x} + t_{i,y} n_{j,y} + t_{i,z} n_{j,z} + d_j \end{bmatrix} \quad (15)$$

Then, by calculating the first-order partial derivative of $\pi'_{i,j}$ with respect to $\mathbf{x}_{i,j}$, $\mathbf{J}_{i,j}^k = \frac{\partial \pi'_{i,j}}{\partial x_k}$ can be obtained. We record the calculation results $\mathbf{J}_{i,j}$ as

$$\mathbf{J}_{i,j} = \begin{bmatrix} \frac{\partial \pi'_{i,j}}{\partial t_i}, \frac{\partial \pi'_{i,j}}{\partial \varphi_i}, \frac{\partial \pi'_{i,j}}{\partial \mathbf{\Pi}_j} \end{bmatrix}^T. \quad (16)$$

where,

$$\frac{\partial \pi'_{i,j}}{\partial \mathbf{t}_i} = \begin{bmatrix} \frac{\partial \pi'_{i,j}}{\partial x_1}, \frac{\partial \pi'_{i,j}}{\partial x_2}, \frac{\partial \pi'_{i,j}}{\partial x_3} \end{bmatrix} = \begin{bmatrix} 0 & 0 & 0 \\ 0 & 0 & 0 \\ 0 & 0 & 0 \\ n_{j,x} & n_{j,y} & n_{j,z} \end{bmatrix} \quad (17)$$

$$\frac{\partial \pi'_{i,j}}{\partial \varphi_i} = \begin{bmatrix} \frac{\partial \pi'_{i,j}}{\partial x_4}, \frac{\partial \pi'_{i,j}}{\partial x_5}, \frac{\partial \pi'_{i,j}}{\partial x_6} \end{bmatrix} = \begin{bmatrix} a & d & g \\ b & e & h \\ c & f & 0 \\ 0 & 0 & 0 \end{bmatrix} \quad (18)$$

$$\frac{\partial \pi'_{i,j}}{\partial \mathbf{\Pi}_j} = \frac{\partial \pi'_{i,j}}{\partial \pi_j} \frac{\partial \pi_j}{\partial \mathbf{\Pi}_j} = \mathbf{T}_i^T \begin{bmatrix} \frac{1}{d_j} (\mathbf{I}_{3 \times 3} - \mathbf{n}_j \mathbf{n}_j^T) \\ \mathbf{n}_j^T \end{bmatrix} \quad (19)$$

To manage the article's length, detailed calculations for formula (18) are provided in the Appendix. The results of $\tilde{\mathbf{G}}_{i,j}^{k,l} = \frac{\partial^2 \pi'_{i,j}}{\partial x_k \partial x_l}$ can be organized as follows

$$\mathbf{G}_{i,j} = \begin{bmatrix} \tilde{\mathbf{G}}_{i,j}^{1,1} & \dots & \tilde{\mathbf{G}}_{i,j}^{1,9} \\ \vdots & \ddots & \vdots \\ \tilde{\mathbf{G}}_{i,j}^{9,1} & \dots & \tilde{\mathbf{G}}_{i,j}^{9,9} \end{bmatrix}_{36 \times 9} = \begin{bmatrix} \vec{0} & \vec{0} & \vec{0} & \vec{0} & \vec{0} & \vec{0} & \vec{a} & \vec{b} & \vec{c} \\ \vec{0} & \vec{0} & \vec{0} & \vec{0} & \vec{0} & \vec{0} & \vec{d} & \vec{e} & \vec{f} \\ \vec{0} & \vec{0} & \vec{0} & \vec{0} & \vec{0} & \vec{0} & \vec{g} & \vec{h} & \vec{i} \\ \vec{0} & \vec{0} & \vec{0} & \vec{j} & \vec{k} & \vec{l} & \vec{p} & \vec{s} & \vec{v} \\ \vec{0} & \vec{0} & \vec{0} & \vec{k} & \vec{m} & \vec{n} & \vec{q} & \vec{t} & \vec{w} \\ \vec{0} & \vec{0} & \vec{0} & \vec{l} & \vec{n} & \vec{o} & \vec{r} & \vec{u} & \vec{x} \\ \vec{a} & \vec{d} & \vec{g} & \vec{p} & \vec{q} & \vec{r} & \vec{y} & \vec{z} & \vec{\alpha} \\ \vec{b} & \vec{e} & \vec{h} & \vec{s} & \vec{t} & \vec{u} & \vec{z} & \vec{\beta} & \vec{\gamma} \\ \vec{c} & \vec{f} & \vec{i} & \vec{v} & \vec{w} & \vec{x} & \vec{\alpha} & \vec{\gamma} & \vec{\eta} \end{bmatrix} \quad (20)$$

The detailed calculation of formula (20) can refer to the Appendix. A similar derivation method is used for the fixed mean square group metric. The estimated values for the fixed mean square group metric is the plane landmark π_j , which can be parameterized as $\mathbf{y}_j = [\Pi_{j,1}, \Pi_{j,2}, \Pi_{j,3}]^T = [y_1, y_2, y_3]^T$. The gradient vector is derived by calculating the first-order partial derivative of c'_j with respect to \mathbf{y}_j

$$g_j^k = \frac{\partial c'_j}{\partial y_k} = \frac{2}{N_j^f} \pi_j^T \mathbf{M}_j \frac{\partial \pi_j}{\partial y_k} \quad (21)$$

Hessian matrix $\mathbf{H}_j = \begin{bmatrix} \ddots & \vdots & \vdots \\ \dots & H_j^{k,l} & \dots \\ \vdots & \vdots & \ddots \end{bmatrix}_{3 \times 3}$ represents the second-order partial derivative of c'_j with respect to \mathbf{y}_j

$$H_j^{k,l} = \frac{\partial^2 c'_j}{\partial y_k \partial y_l} = \frac{2}{N_j^f} \left(\frac{\partial \pi_j}{\partial y_l} \mathbf{M}_j \frac{\partial \pi_j}{\partial y_k} + \pi_j^T \mathbf{M}_j \frac{\partial^2 \pi_j}{\partial y_k \partial y_l} \right) \quad (22)$$

By calculating the first-order partial derivative of π_j with respect to \mathbf{y}_j , $\mathbf{J}_j^k = \frac{\partial \pi_j}{\partial y_k}$ can be obtained. We record the calculation results as

$$\mathbf{J}_j = \begin{bmatrix} \frac{\partial \pi_j}{\partial y_1}, \frac{\partial \pi_j}{\partial y_2}, \frac{\partial \pi_j}{\partial y_3} \end{bmatrix} = \frac{\partial \pi_j}{\partial \mathbf{\Pi}_j} \quad (23)$$

Then, the results of $\tilde{\mathbf{G}}_j^{k,l} = \frac{\partial^2 \pi_j}{\partial y_k \partial y_l}$ can be defined as

$$\mathbf{G}_j = \begin{bmatrix} \tilde{\mathbf{G}}_j^{1,1} & \tilde{\mathbf{G}}_j^{1,2} & \tilde{\mathbf{G}}_j^{1,3} \\ \tilde{\mathbf{G}}_j^{2,1} & \tilde{\mathbf{G}}_j^{2,2} & \tilde{\mathbf{G}}_j^{2,3} \\ \tilde{\mathbf{G}}_j^{3,1} & \tilde{\mathbf{G}}_j^{3,2} & \tilde{\mathbf{G}}_j^{3,3} \end{bmatrix} = \begin{bmatrix} \vec{a}^f & \vec{b}^f & \vec{c}^f \\ \vec{b}^f & \vec{d}^f & \vec{e}^f \\ \vec{c}^f & \vec{e}^f & \vec{f}^f \end{bmatrix} \quad (24)$$

For a detailed calculation of formula (24), please refer to the Appendix. Finally, we need to derive the Hessian matrix and gradient vector considering $\rho(\cdot)$. We will use c in the following representation since $c'_{i,j}$ and c'_j share the same processing methods. The estimated values are defined as \mathbf{x} . By performing Taylor expansion on $\rho(c)$ and retaining terms up to the second order, we obtain

$$\rho(c) = const + \rho' \Delta c + \frac{1}{2} \rho'' \Delta c^2 \quad (25)$$

where, $const$ represents the constant. ρ' and ρ'' denote the first and second derivatives of $\rho(c)$ with respect to the metric c , respectively. The incremental metric Δc has the following form

$$\Delta c = c(\mathbf{x} + \Delta \mathbf{x}) - c(\mathbf{x}) = \mathbf{J} \Delta \mathbf{x} + \frac{1}{2} \Delta \mathbf{x}^T \mathbf{H} \Delta \mathbf{x} \quad (26)$$

Substituting formula (26) into formula (25), we obtain

$$\begin{aligned} \rho(c) &= const + \rho' \Delta c + \frac{1}{2} \rho'' \Delta c^2 \\ &\approx const + \rho' \mathbf{J} \Delta \mathbf{x} + \frac{1}{2} \rho' \Delta \mathbf{x}^T \mathbf{H} \Delta \mathbf{x} + \frac{1}{2} \rho'' \Delta \mathbf{x}^T \mathbf{J}^T \mathbf{J} \Delta \mathbf{x} \\ &= const + \rho' \mathbf{J} \Delta \mathbf{x} + \frac{1}{2} \Delta \mathbf{x}^T (\rho' \mathbf{H} + \rho'' \mathbf{J}^T \mathbf{J}) \Delta \mathbf{x} \end{aligned} \quad (27)$$

Derive the formula (27) from $\Delta \mathbf{x}$ and set it equal to zero. The resulting normal equation, taking into account robust kernel functions, is as follows:

$$(\rho' \mathbf{H} + \rho'' \mathbf{J}^T \mathbf{J}) \Delta \mathbf{x} = -\rho' \mathbf{J}^T \quad (28)$$

By applying normal equation calculations on each metric in formula (7), we can construct an estimation model similar to the visual BA model. The Schur complement technique [11] is employed to accelerate the solution.

IV. INTEGRATED SYSTEM

This section will present a loosely coupled SLAM system that integrates the proposed RSO-BA estimator. The system's front end can calculate the odometry pose and undistorted point cloud of the current frame. If the current frame is identified as a keyframe, it will be inserted into the system's backend. The RSO-BA estimator is then used to refine the map. The system flowchart is shown in Figure 1.

A. Front End

Assuming the odometry coordinate system is o . The system's front end uses the Fast-LIO2 [1] module to process the raw measurement point cloud and IMU data. A local point cloud map is maintained using the ikd-tree [27] data structure. The distortion in the raw point cloud ψ_i is corrected using with a bidirectional propagation algorithm based on the IMU sensor. The IEKF [20] estimator is then used to register the

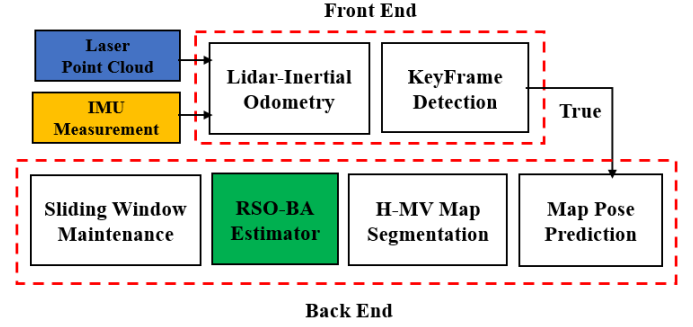


Fig. 1: System flowchart. The green box represents the proposed explicit second-order BA estimator.

undistorted point cloud $\bar{\psi}_i$ to the local point cloud map. The estimated odometry pose for the current LiDAR frame is $\mathbf{T}_{ol,i}$.

Then, keyframe detection is performed based on the following conditions:

- (1) The difference in timestamps between the current frame and the last keyframe exceeds the threshold th_{time} .
- (2) The 2-norm of the translation increment or the 2-norm of the rotation increment, compared to the last keyframe, is greater than th_{pos} or th_{deg} , respectively.

If both conditions are met, $\bar{\psi}_i$ and $\mathbf{T}_{ol,i}$ are used to create the current keyframe \mathbb{F}_k . The keyframe \mathbb{F}_k is then inserted into the system's backend.

B. Back End

The system's backend employs the hash adaptive voxel map (H-AV) proposed by BALM [6] for global map maintenance. Similar to LOAM [4], we maintain a corrected transformation \mathbf{T}_{mo} from odometry coordinate system o to map coordinate system m . Based on the odometry pose \mathbf{T}_{ol} calculated by the front end and the latest corrected transformation \mathbf{T}_{mo} , the predicted pose \mathbf{T}'_{ml} in the map coordinate system can be defined

$$\mathbf{T}'_{ml} = \mathbf{T}_{mo} \mathbf{T}_{ol} \quad (29)$$

The 9-value sampling algorithm [28] is used to extract a fixed number of plane feature point set $\bar{\Phi}_k$ with complete pose constraints from $\bar{\psi}_k$. The current keyframe \mathbb{F}_k storing $\bar{\psi}_k$ and \mathbf{T}'_{ml} is created and inserted into a sliding window. Then, we use \mathbf{T}'_{ml} to insert $\bar{\psi}_k$ into the H-AV map and perform adaptive voxel segmentation. When the number of keyframes in the sliding window reaches th_{kf} , the RSO-BA estimator proposed in Section III.C is used to perform map refinement. \mathbf{T}_{mo} is corrected by the optimized keyframe pose \mathbf{T}_{ml} and odometry pose \mathbf{T}_{ol}

$$\mathbf{T}_{mo} = \mathbf{T}_{ml} \mathbf{T}_{ol}^{-1} \quad (30)$$

Finally, the measurement information corresponding to each landmark in the oldest keyframe is marginalized to the fixed group matrix, after which the oldest keyframe is removed from the sliding window.

V. EXPERIMENT

This section will verify the effectiveness of the proposed RSO-BA algorithm. All experiments were conducted on the AMD ® Ryzen 7 5800h (8 cores @ 3.2 GHz), 16GB RAM, ROS Melodic environment. The experiment is divided into two parts: structured scene experiments and unstructured scene experiments. The specific experimental setup and result analysis are as follows.

A. Experimental Setup

For the other BA algorithms involved in the experiment, BALM2 [7] is an improved version based on BALM [6]. BALM2 introduces a two-step BA algorithm that iteratively performs eigenvalue fitting and multi-view pose registration. The multi-view pose registration is achieved using a second-order Newton estimator. By introducing the concept of "point clustering", the Hessian matrix and gradient vector can be calculated as a "group", effectively avoiding the time-consuming process of point-by-point calculation. Unlike BALM2, PA [9] estimates plane landmarks and poses simultaneously. This algorithm uses QR decomposition to calculate the reduction error vector and the reduction Jacobian matrix. Then, an approximate second-order algorithm based on LM [29] was used for updating state variables.

In the structured scene experiment, we validated the proposed algorithm using the SLAM system developed in Section IV. For the indoor Hilti [30] dataset, the measurement point cloud resolution r^{mea} and ikd-tree map resolution r^{ikd} in Fast-LIO2 are set to 0.4 m and 0.2 m, respectively. The keyframe detection conditions are $th_{time} = 0.25s$, $th_{pos} = 0.1m$, and $th_{deg} = 0.05^\circ$. The maximum depth and maximum voxel resolution of the Hash Adaptive Voxel (H-AV) map are $d_{max} = 4$ and $r_{max}^{hav} = 1m$. The number of keyframes in the sliding window is set to $th_{kf} = 10$. For the outdoor UrbanNav [31] dataset, the measurement point cloud resolution r^{mea} and map resolution r^{ikd} are both set to 0.5 m. The keyframe detection remains the same as above. The maximum depth of the H-AV map is $d_{max} = 3$, and the maximum voxel resolution is $r_{max}^{hav} = 2m$. The number of keyframes in the sliding window is consistent with the indoor experiment.

We also compared the performance of different BA algorithms in unstructured scenes using the ETHZ [32] dataset. The initial pose estimation method for the LiDAR frame is detailed in Section V.C The backend parameter settings are the same as those on the Hilti [30] dataset. To ensure a fair comparison, all BA estimators in the experiment are iteratively optimized using the LM [29] algorithm. The damping factor λ for all algorithm is set to 0.01 with a maximum of 20 iterations. For the indoor Hilti and ETHZ point cloud registration datasets, the Huber kernel function threshold of the RSO-BA algorithm is set to 0.02. For the outdoor UrbanNav dataset, the threshold is set to 0.1.

B. Structured Scene Experiment

In this section, we conduct experiments using the indoor Hilti [30] dataset and the outdoor UrbanNav [31] dataset to

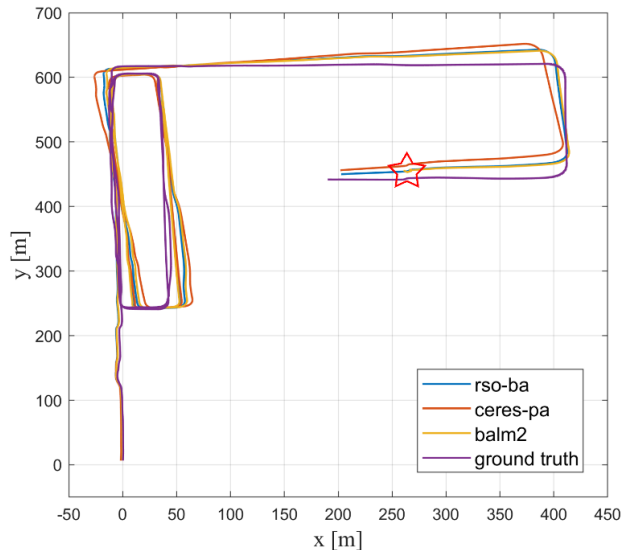


Fig. 2: The running trajectories of different BA algorithms under UrbanNav Mongkok sequence. The accuracy of PA is much lower than that of RSO-BA and BALM2. BALM2 experienced severe trajectory drift at the location marked by the red star..

evaluate the registration accuracy of different BA algorithms using the ATE [33] metric. The Hilti dataset includes raw point clouds collected by Ouster Os0-64 or Hesai PandarXT-32 LiDAR, along with acceleration and angular velocity data collected by an Analog Devices ADIS1644 inertial measurement unit. Data collection was conducted in static scenarios such as laboratories and offices. The UrbanNav dataset provides raw point clouds collected by a Velodyne HDL-32E LiDAR, along with acceleration and angular velocity data from an Xsens Mti 10 inertial measurement unit. The dataset was collected in Hong Kong and involves numerous moving vehicles, which can easily disrupt the stability of the system's front end. Figures 2 show the robot trajectories of different BA algorithms on the UrbanNav dataset.

Tables 1 and 2 demonstrate that the proposed RSO-BA algorithm achieved the best ATE accuracy in most sequences. Among all successful sequences, it is evident that the estimation accuracy of RSO-BA and BALM2 is significantly better than that of PA. The primary reason for the superior performance of RSO-BA and BALM2 is that both estimators utilize a second-order Newton's method, which leverages second-order

TABLE I: Registration accuracy under the Hilti dataset.

| Absolute Motion Trajectory RMSE [cm] | | | |
|--------------------------------------|-------------|------------|------------|
| Sequence | BALM2 | PA | RSO-BA |
| LAB_2 | 1.4 | 2.5 | 1.3 |
| uzh_run2 | 16.8 | 25.4 | 16.9 |
| exp04_level | 2.1 | 2.0 | 2.0 |
| exp05_level_2 | - | 2.1 | 2.1 |
| exp06_level_3 | - | 3.9 | 2.7 |
| exp14_basement_2 | - | 6.6 | 3.5 |
| Mean | - | 7.1 | 4.8 |

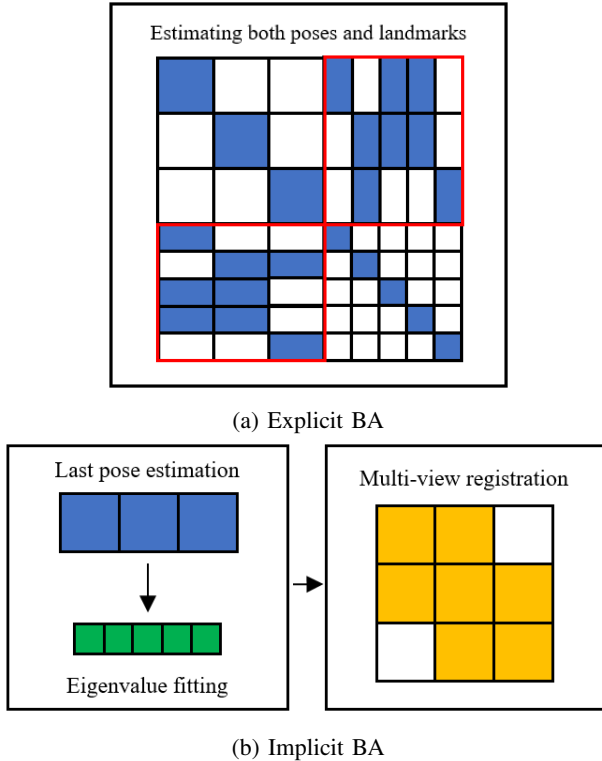


Fig. 3: Single iteration of different BA algorithms.

terms to achieve better convergence performance. Additionally, compared to BALM2, RSO-BA offers certain advantages in registration accuracy. This is because, in BALM2’s two-step estimation process, eigenvalue fitting (landmark estimation) is based solely on the multi-view pose and measurement information from the previous step. This approach overlooks the interaction between pose and landmarks during the current state update process (highlighted in the red box in Figure 3(a)), an interaction that is explicitly accounted for in the RSO-BA algorithm.

TABLE II: Registration accuracy under the UrbanNav dataset.

| Absolute Motion Trajectory RMSE [m] | | | |
|-------------------------------------|-------|-------|-------------|
| Sequence | BALM2 | PA | RSO-BA |
| HK-Mongkok | 7.11 | 12.77 | 6.77 |
| HK-TST | - | 12.1 | 8.97 |
| HK-Whampoa | - | 9.89 | 6.83 |
| Mean | - | 11.58 | 7.52 |

On the other hand, we observed that BALM2 failed to run in multiple sequences. One possible reason is that the BALM2 algorithm requires the current multi-view pose for landmark estimation at the first step in each iteration. If the initial value provided by the front-end pose is poor, the landmark parameters may not be able to converge to a better state, leading to divergent estimation results. In contrast, the RSO-BA and PA algorithms, which estimate landmarks and poses simultaneously, can leverage the constraints between them. This makes the estimation model more robust, allowing it to successfully execute across all sequences.

C. Unstructured Scene Experiment

The ETHZ [32] point cloud registration dataset statically collected measurement point clouds using the Hokuyo UTM-30LX LiDAR. This dataset includes a range of complex scenarios, from structured environments like apartments to unstructured settings like forests. Unstructured scenarios present challenges for feature-based BA schemes. Since the measurement point clouds do not require motion distortion correction, we utilize the point-to-plane error metric proposed by [14] and the scan-to-map registration method to estimate the initial odometry pose required for the system’s backend. The map is maintained incrementally using the ikd-tree data structure. Given that all measurement point clouds are captured from independent perspectives, we directly insert the measurement point clouds and estimated pose into the backend without performing keyframe detection.

TABLE III: Registration accuracy under the ETHZ dataset.

| Absolute Motion Trajectory RMSE [cm] | | | |
|--------------------------------------|------------|------------|------------|
| Sequence | BALM2 | PA | RSO-BA |
| apartment | 0.8 | 1.3 | 0.8 |
| hauptgebaude | 0.4 | 0.6 | 0.5 |
| gazebo_summer | 1.7 | 11.2 | 1.4 |
| gazebo_winter | 8.6 | 3.1 | 1.1 |
| mountain_plain | 12.1 | 6.1 | 6.9 |
| stairs | 1.2 | 1.1 | 0.9 |
| wood_autumn | 2.0 | 2.4 | 1.5 |
| wood_summer | 1.8 | 3.1 | 1.7 |
| Mean | 3.5 | 3.6 | 1.8 |

Table 3 presents the ATE evaluation results for three BA algorithms. In structured scenes such as apartments and stairs, the registration accuracy of the proposed RSO-BA and BALM2 algorithms is nearly equivalent and significantly better than that of the PA algorithm, consistent with the findings in Section 5.2. However, in unstructured scenes such as mountain and woods, the RSO-BA algorithm significantly outperforms both BALM2 and PA. This improvement is due to the RSO-BA algorithm’s use of a robust kernel function to reweight all measurements. The measurements corresponding to flatter plane landmarks have a greater weight in the optimization process, which enhances estimation accuracy.

TABLE IV: Map quality evaluation under the ETHZ dataset.

| Voxel occupancy number | | | |
|------------------------|--------------|--------------|---------------|
| Sequence | BALM2 | PA | RSO-BA |
| apartment | 56910 | 57664 | 57011 |
| hauptgebaude | 225853 | 225812 | 225671 |
| gazebo_summer | 155449 | 182999 | 154424 |
| gazebo_winter | 195433 | 197637 | 177688 |
| mountain_plain | 92149 | 90087 | 90744 |
| stairs | 88501 | 88675 | 88169 |
| wood_autumn | 349279 | 346779 | 346219 |
| wood_summer | 411731 | 410541 | 409234 |
| Mean | 196913 | 200024 | 193645 |

Table 4 presents the quality evaluation of the reconstructed maps using the voxel occupancy [34] method. During the experiment, we set the voxel size to 0.1m. The higher the

quality of map reconstruction (and the more accurate the sensor pose estimation), the fewer voxels the point cloud map occupies. The average voxel occupancy number of the RSO-BA algorithm is significantly lower than that of the other two BA algorithms. Additionally, the map quality evaluation results in Table 4 are consistent with the registration accuracy evaluation results shown in Table 3.

VI. CONCLUSIONS AND FUTURE WORK

In this article, we propose a novel LiDAR bundle adjustment algorithm based on the mean square group metric. Leveraging the mean square group metric with scale interpretability, the robust BA model can be built using a robust kernel function. We then derive the analytical Hessian matrix and gradient vector required for the second-order estimator (RSO-BA) to enhance estimation accuracy. The proposed RSO-BA estimator is compared with other advanced LiDAR BA algorithms, such as BALM2 and PA, on publicly available datasets. Experimental results demonstrate that the RSO-BA estimator offers superior robustness and estimation accuracy in complex scenarios, including unstructured and highly dynamic environments. However, the pure LiDAR BA algorithm tends to degrade in weakly textured scenes, such as long corridors, leading to significant trajectory drift. As a high-frequency, internal sensing sensor, the inertial measurement unit (IMU) can effectively overcome the above problems. In the future, we plan to explore the multi-sensor fusion BA estimation algorithm to improve the system's adaptability across diverse environments.

REFERENCES

- [1] W. Xu, Y. Cai, D. He, J. Lin, and F. Zhang, "Fast-lio2: Fast direct lidar-inertial odometry," *IEEE Transactions on Robotics*, vol. 38, no. 4, pp. 2053–2073, 2022.
- [2] P. Dellenbach, J.-E. Deschaud, B. Jacquet, and F. Goulette, "Ct-icp: Real-time elastic lidar odometry with loop closure," in *2022 International Conference on Robotics and Automation (ICRA)*. IEEE, 2022, pp. 5580–5586.
- [3] T. Shan and B. Englot, "Lego-loam: Lightweight and ground-optimized lidar odometry and mapping on variable terrain," in *2018 IEEE/RSJ International Conference on Intelligent Robots and Systems (IROS)*. IEEE, 2018, pp. 4758–4765.
- [4] J. Zhang and S. Singh, "Loam: Lidar odometry and mapping in real-time," in *Robotics: Science and Systems*, vol. 2, no. 9. Berkeley, CA, 2014, pp. 1–9.
- [5] J. Lin and F. Zhang, "Loam livox: A fast, robust, high-precision lidar odometry and mapping package for lidars of small fov," in *2020 IEEE international conference on robotics and automation (ICRA)*. IEEE, 2020, pp. 3126–3131.
- [6] Z. Liu and F. Zhang, "Balm: Bundle adjustment for lidar mapping," *IEEE Robotics and Automation Letters*, vol. 6, no. 2, pp. 3184–3191, 2021.
- [7] Z. Liu, X. Liu, and F. Zhang, "Efficient and consistent bundle adjustment on lidar point clouds," *IEEE Transactions on Robotics*, 2023.
- [8] L. Zhou, D. Koppel, H. Ju, F. Steinbruecker, and M. Kaess, "An efficient planar bundle adjustment algorithm," in *2020 IEEE International Symposium on Mixed and Augmented Reality (ISMAR)*. IEEE, 2020, pp. 136–145.
- [9] L. Zhou, D. Koppel, and M. Kaess, "Lidar slam with plane adjustment for indoor environment," *IEEE Robotics and Automation Letters*, vol. 6, no. 4, pp. 7073–7080, 2021.
- [10] P. Geneva, K. Eckenhoff, Y. Yang, and G. Huang, "Lips: Lidar-inertial 3d plane slam," in *2018 IEEE/RSJ International Conference on Intelligent Robots and Systems (IROS)*. IEEE, 2018, pp. 123–130.
- [11] B. Triggs, P. F. McLauchlan, R. I. Hartley, and A. W. Fitzgibbon, "Bundle adjustment—a modern synthesis," in *Vision Algorithms: Theory and Practice: International Workshop on Vision Algorithms Corfu, Greece, September 21–22, 1999 Proceedings*. Springer, 2000, pp. 298–372.
- [12] C. Zach, "Robust bundle adjustment revisited," in *Computer Vision—ECCV 2014: 13th European Conference, Zurich, Switzerland, September 6–12, 2014, Proceedings, Part V 13*. Springer, 2014, pp. 772–787.
- [13] P. J. Besl and N. D. McKay, "Method for registration of 3-d shapes," in *Sensor fusion IV: control paradigms and data structures*, vol. 1611. Spie, 1992, pp. 586–606.
- [14] Y. Chen and G. Medioni, "Object modelling by registration of multiple range images," *Image and vision computing*, vol. 10, no. 3, pp. 145–155, 1992.
- [15] H. Hotelling, "Analysis of a complex of statistical variables into principal components," *Journal of educational psychology*, vol. 24, no. 6, p. 417, 1933.
- [16] A. Segal, D. Haehnel, and S. Thrun, "Generalized-icp," in *Robotics: science and systems*, vol. 2, no. 4. Seattle, WA, 2009, p. 435.
- [17] K. Koide, M. Yokozuka, S. Oishi, and A. Banno, "Voxelized gicp for fast and accurate 3d point cloud registration," in *2021 IEEE International Conference on Robotics and Automation (ICRA)*. IEEE, 2021, pp. 11 054–11 059.
- [18] J. Serafin and G. Grisetti, "Nipc: Dense normal based point cloud registration," in *2015 IEEE/RSJ International Conference on Intelligent Robots and Systems (IROS)*. IEEE, 2015, pp. 742–749.
- [19] T. Shan, B. Englot, D. Meyers, W. Wang, C. Ratti, and D. Rus, "Lio-sam: Tightly-coupled lidar inertial odometry via smoothing and mapping," in *2020 IEEE/RSJ international conference on intelligent robots and systems (IROS)*. IEEE, 2020, pp. 5135–5142.
- [20] B. M. Bell and F. W. Cathey, "The iterated kalman filter update as a gauss-newton method," *IEEE Transactions on Automatic Control*, vol. 38, no. 2, pp. 294–297, 1993.
- [21] R. Beran, "Robust location estimates," *The Annals of Statistics*, pp. 431–444, 1977.
- [22] M. J. Black and A. Rangarajan, "On the unification of line processes, outlier rejection, and robust statistics with applications in early vision," *International journal of computer vision*, vol. 19, no. 1, pp. 57–91, 1996.
- [23] T. Qin, P. Li, and S. Shen, "Vins-mono: A robust and versatile monocular visual-inertial state estimator," *IEEE transactions on robotics*, vol. 34, no. 4, pp. 1004–1020, 2018.
- [24] S. Leutenegger, P. Furgale, V. Rabaud, M. Chli, K. Konolige, and R. Siegwart, "Keyframe-based visual-inertial slam using nonlinear optimization," *Proceedings of Robotics Science and Systems (RSS) 2013*, 2013.
- [25] R. Kümmerle, G. Grisetti, H. Strasdat, K. Konolige, and W. Burgard, "g 2 o: A general framework for graph optimization," in *2011 IEEE international conference on robotics and automation*. IEEE, 2011, pp. 3607–3613.
- [26] C. F. Gauss, *Theoria motus corporum coelestium in sectionibus conicis solem ambientium*. FA Perthes, 1877, vol. 7.
- [27] Y. Cai, W. Xu, and F. Zhang, "ikd-tree: An incremental kd tree for robotic applications," *arXiv preprint arXiv:2102.10808*, 2021.
- [28] J.-E. Deschaud, "Imls-slam: Scan-to-model matching based on 3d data," in *2018 IEEE International Conference on Robotics and Automation (ICRA)*. IEEE, 2018, pp. 2480–2485.
- [29] A. Ranganathan, "The levenberg-marquardt algorithm," *Tutorial on LM algorithm*, vol. 11, no. 1, pp. 101–110, 2004.
- [30] M. Helmberger, K. Morin, B. Berner, N. Kumar, G. Cioffi, and D. Scaramuzza, "The hilti slam challenge dataset," *IEEE Robotics and Automation Letters*, vol. 7, no. 3, pp. 7518–7525, 2022.
- [31] L.-T. Hsu, N. Kubo, W. Wen, W. Chen, Z. Liu, T. Suzuki, and J. Meguro, "Urbannav: An open-sourced multisensory dataset for benchmarking positioning algorithms designed for urban areas," in *Proceedings of the 34th international technical meeting of the satellite division of the institute of navigation (ION GNSS+ 2021)*, 2021, pp. 226–256.
- [32] F. Pomerleau, M. Liu, F. Colas, and R. Siegwart, "Challenging data sets for point cloud registration algorithms," *The International Journal of Robotics Research*, vol. 31, no. 14, pp. 1705–1711, 2012.
- [33] J. Sturm, N. Engelhard, F. Endres, W. Burgard, and D. Cremers, "A benchmark for the evaluation of rgb-d slam systems," in *2012 IEEE/RSJ international conference on intelligent robots and systems*. IEEE, 2012, pp. 573–580.
- [34] A. Filatov, A. Filatov, K. Krinkin, B. Chen, and D. Molodan, "2d slam quality evaluation methods," in *2017 21st Conference of Open Innovations Association (FRUCT)*. IEEE, 2017, pp. 120–126.